Large eddy simulation/probability density function modeling of turbulent swirling stratified flame series ⓔ⅀

ⓘⅅ **Hasret Turkeri**, **Xinyu Zhao**, and ⓘⅅ **Metin Muradoglu**

COLLECTIONS

Paper published as part of the special topic on In Memory of Edward E. (Ted) O'Brien

Ⓔⅅ   This paper was selected as an Editor's Pick

View Online   Export Citation   CrossMark

ARTICLES YOU MAY BE INTERESTED IN

Experimental study of the effect of outlet boundary on combustion instabilities in premixed swirling flames
Physics of Fluids **33**, 027106 (2021); https://doi.org/10.1063/5.0038984

Convolutional neural network and long short-term memory based reduced order surrogate for minimal turbulent channel flow
Physics of Fluids **33**, 025116 (2021); https://doi.org/10.1063/5.0039845

Numerical study of virus transmission through droplets from sneezing in a cafeteria
Physics of Fluids **33**, 023311 (2021); https://doi.org/10.1063/5.0040803

Large eddy simulation/probability density function modeling of turbulent swirling stratified flame series ⓔⓟ

View Online   Export Citation   CrossMark

Hasret Turkeri,[1,a)] ⓘⅅ Xinyu Zhao,[2] and Metin Muradoglu[3] ⓘⅅ

AFFILIATIONS

[1]Tusas Engine Industries (TEI), Inc., Eskisehir 26210, Turkey
[2]Department of Mechanical Engineering, University of Connecticut, Storrs, Connecticut 06269, USA
[3]Department of Mechanical Engineering, Koç University, Rumelifeneri Yolu, Sariyer, 34450 Istanbul, Turkey

Note: This paper is part of the Special Topic, In Memory of Edward E. (Ted) O'Brien.
[a)]Author to whom correspondence should be addressed: hturkeri@ku.edu.tr and hasretturkeri@gmail.com

ABSTRACT

The large eddy simulation/probability density function (LES/PDF) method is applied to a turbulent swirling stratified flame series to systematically investigate its performance for accurate prediction of effects of stratification on turbulent flames under swirling conditions. The Cambridge/Sandia turbulent stratified flame series is selected as a target flame series. An augmented reduced mechanism is used for the methane/air combustion. The chemical calculations are accelerated by using the *in situ* adaptive tabulation method. The differential diffusion and heat loss from the bluff-body surface are taken into account in the simulations. The effect of stratification in fuel concentration is studied by increasing the stratification progressively from the pure premixed case to moderately and highly stratified cases. The performance of the LES/PDF modeling is evaluated by comparing the numerical results with the experimental data. The computed mean and rms of velocity, temperature, equivalence ratio, and mass fractions of species are found to be in good agreement with the measurements for all three conditions. Scatter plots and conditional means of mole fractions of species and temperature are presented and found to be in overall good consistency with those obtained from the experimental measurements. The recirculation zones are found to be about five times longer than those obtained under the non-swirling conditions. A low-equivalence-ratio high-temperature region near the bluff body is not captured in the computation, which is attributed to the insufficient entrainment of downstream mixtures into the recirculation zone. The parametric studies show that the differential diffusion has a minor effect on the mean and rms quantities, while the heat loss has a considerable effect on temperature and CO profiles close to the bluff body.

Published under license by AIP Publishing. https://doi.org/10.1063/5.0039810

I. INTRODUCTION

Swirling flow is widely used to stabilize lean premixed turbulent flames in gas turbines to satisfy the low-emission constraints and to reduce the size of the combustion devices by increasing the residence time.[1] Despite its effectiveness, swirling flows introduce significant challenges in terms of combustion instabilities because they are primarily characterized by low frequency large-scale coherent flow structures that are inherently unstable. These unstable flow patterns increase the turbulent intensity and also introduce combustion oscillations, which makes it challenging to model the interaction between turbulence and chemistry.[2,3] Additionally, in many combustion engines, the combustion occurs in a partially premixed mode mainly due to the insufficient time and length scales for fuel to mix with air

perfectly. The inhomogeneous fuel distribution in the combustible mixture may lead to combustion instabilities due to strong fluctuation in the heat release rate.[4] The combined effects of stratified combustion under swirling conditions introduce challenges to the numerical modeling of turbulent flames. Therefore, it is vitally important to assess the performance of turbulence and combustion models using the well-defined benchmark experimental data for turbulent stratified flames under swirling conditions.

A number of numerical studies have been performed for partially premixed swirling turbulent flames using various combustion models.[5–11] These studies mainly focus on gas turbine model combustors (GTMCs) with different degrees of stratification in fuel concentrations.[4,12–14] Such GTMC configurations usually include the plenum,

swirler, and combustor walls, which often introduce additional complexities to the model validation process.

To avoid such complexities and to accelerate the model validation process, many canonical swirl burners are designed. For example, Bonaldo and Kelman[15] have developed a weak swirl lean stratified premixed burner in an unconfined atmosphere. The stratification is provided by two concentric annular flow jets feeding the fuel with different equivalence ratios. The swirling coflow air is provided to stabilize the flame with a minimal swirl. The weak swirl is insufficient to create a recirculation zone; however, it leads the mean axial velocity to decay almost linearly. Consequently, the flame is stabilized at the position where the velocity of the fresh fuel mixture is equal to the flame speed. Nogenmyr et al.[16–18] developed a laboratory measurement rig where a premixed CH_4/air mixture is injected through a low swirl burner into a low speed co-flowing air at room temperature and pressure. The flame is stabilized in a low velocity region above the burner created by the swirling flow. The stratification in fuel concentration occurs due to the dilution of the ambient air in the shear layer, while the flame core remains premixed. The authors have also modeled the flame using the G-equation model employing two different chemistry models, i.e., flamelet and finite-rate chemistry. The two chemistry models have predicted similar mean and rms flow fields, while the finite-rate chemistry model resulted in closer agreement with the experiments.

Recently, the Cambridge/Sandia swirl burner has been developed by Sweeney et al.[19,20] to investigate stratified turbulent flames under both swirling and non-swirling conditions and to provide detailed experimental measurements for validation of numerical models. The burner has a central bluff body, two annular fuel streams, and an air coflow. The fuel/air mixtures stream from two annular jets at different equivalence ratios. Several numerical studies have been conducted for the flame series under non-swirling conditions using different combustion models: a filtered-laminar-flame probability density function (PDF) model,[21,22] an artificial thickened flame model,[23] a probability density function (PDF) model employing the Eulerian stochastic field method,[24] and a transported PDF model.[25]

The burner under swirling conditions has also been modeled using different combustion models. Brauner et al.[24] reported numerical results for the stratified turbulent flames under the swirling conditions. In their study, the flow fields have been predicted quite accurately; however, the numerical predictions of species show apparent discrepancies within the recirculation zone. Additionally, temperature is over-predicted within the recirculation zone and close to the bluff body. Zhang et al.[26] studied the burner in the premixed mode under both swirling and non-swirling conditions using two different combustion models, including the dynamic thickened flame model with tabulated detailed chemistry and the presumed-PDF model with tabulated detailed chemistry. In this study, although the mean temperature and species profiles are in reasonable agreement with the experimental data, the rms profiles are lower than the measurements. Xiao et al.[27] performed a numerical study using the partially stirred reactor (PaSR) model. Although the trends in the experimental data have been captured by the numerical results, the magnitudes of the mean temperature and main products are predicted to be lower than the measurements. Gruhlke et al.[28] conducted a numerical study for the burner in the premixed mode using a dynamic thickened flame approach with a new post-processing method for finite-rate chemistry.

The new post-processing method improves the prediction of minor species such as CO. Subsequently, Mercier et al.[29] modeled the burner in the premixed mode under the swirling conditions using the filtered wrinkled flamelet model. The mean temperature profiles have been over-predicted within the recirculation zone. Additionally, the mean CO profiles have shown discrepancies compared to the measurements.

The performance of the large eddy simulation (LES)/PDF methodology for calculating the effects of stratification in fuel concentration under the non-swirling conditions has been presented in our previous study.[25] The main objective of the present computational study is to assess the predictive capability of the method for accurate modeling of stratification effects on turbulent flames under the swirling conditions. Additionally, this study aims to investigate the effect of heat loss through the bluff body and the effect of the differential diffusion under the swirling conditions. For this purpose, the Cambridge/Sandia turbulent stratified flame series is selected as target flames. The transported PDF method has proven to be an efficient model in non-premixed,[30–33] premixed,[34–36] and partially premixed[37] combustion modes mainly because the highly non-linear chemical source term appears to be in a closed form.

This paper is structured as follows: In Sec. II, the LES/PDF method is presented. A summary of the configurations of the burner and the numerical setup is provided in Sec. III. The results are presented and discussed in Sec. IV. Conclusions are drawn in Sec. V.

II. METHODOLOGY

In the LES/PDF methodology, LES is employed to solve for the turbulent flow field, while the PDF method is employed to treat the turbulence–chemistry interactions. The details of the present LES/PDF method have been presented in our previous papers.[25,38] The main features of the method are summarized here for the sake of completeness.

A. Governing equations

In the LES method, the turbulent fields are separated into large and small scales by applying a low bandpass filtering operation. For example, the filtered density field $\overline{\rho}$ is defined as

$$\overline{\rho}(\boldsymbol{x}, t) \equiv \int_{-\infty}^{\infty} \rho(\boldsymbol{y}, t) G(\boldsymbol{y} - \boldsymbol{x}) d\boldsymbol{y}, \tag{1}$$

where $\rho(\boldsymbol{x}, t)$ is the density field and G is the LES filter. The filtered transport equations for mass and momentum are obtained by applying the LES filter to the instantaneous mass and momentum conservation equations. Then, the one-equation eddy-viscosity model[39] is used to model the effects of the sub-grid scale stresses as discussed in detail by Turkeri et al.[25,38]

In the PDF method employing a Monte Carlo approach, the flow is represented by notional Lagrangian particles. The particles evolve in physical and compositional space according to the following stochastic differential equations:[40]

$$dX_j^* = \left(\tilde{u}_j + \frac{1}{\overline{\rho}} \frac{\partial(\overline{\rho}\tilde{D}_T)}{\partial x_j} \right)^* dt + \left(2\tilde{D}_T^* \right)^{1/2} dW_j^*, \tag{2}$$

$$\frac{d\phi_\alpha^*}{dt} = -\Omega^* \left(\phi_\alpha^* - \tilde{\phi}_\alpha^* \right) + \left[\frac{1}{\overline{\rho}} \frac{\partial \overline{\rho} V_{\alpha,i}}{\partial x_i} \right]^* + S_\alpha(\phi^*), \tag{3}$$

where the superscript "*" indicates the particle properties or the LES fields interpolated at the particle locations. The first term on the right hand side of Eq. (3) accounts for the molecular mixing using the IEM mixing model, whereas the second term is the mean drift term. In Eq. (2), dW_j^* is the Wiener increment in the j direction. $\tilde{u}_j$ and $\tilde{D}_T$ are the Favre-filtered velocity and the turbulent diffusivity, respectively. ϕ_α^* represents the particle properties of species mass fraction and the sensible enthalpy. $V_{\alpha,i}$ is a corrected diffusion velocity defined in Ref. 25. S_α is a chemical source term for the particle property of α. Finally, Ω^* is the molecular mixing term, which is modeled as

$$\Omega^* = C_m \frac{\tilde{D}^* + \tilde{D}_T^*}{\Delta^2}, \qquad (4)$$

where C_m is a model constant. The value of C_m is determined based on a sensitivity study by matching the computed statistics with the experimental data.[25] $\tilde{D}^*$ is the thermal diffusivity, and Δ is the LES filter size. In this study, the transport properties such as the molecular viscosity and the thermal and species diffusivities are calculated using CHEMKIN's transport library.[41]

The solution of the LES/PDF model equations is achieved using a hybrid method such that the finite-volume method is used to solve the filtered conservation equations of mass and momentum, while a Monte Carlo approach is employed to evolve the Lagrangian particle properties. The details of the hybrid method have been presented in Ref. 38. The coupling of the Lagrangian Monte Carlo method and Eulerian finite-volume method is achieved by employing the transported specific volume (TSV) method.[42] In this method, a transport equation for the Favre-filtered specific volume $\tilde{v}$ is solved, which has the following form:

$$\frac{\partial \overline{\rho}\tilde{v}}{\partial t} + \frac{\partial (\overline{\rho}\tilde{u}_j\tilde{v})}{\partial x_j} = \frac{\partial}{\partial x_j}\left(\overline{\rho}\tilde{D}_T \frac{\partial \tilde{v}}{\partial x_j}\right) + S_v + \dot{\omega}_v, \qquad (5)$$

where S_v is a source term calculated by the Monte Carlo solver and represents the change of Favre-filtered specific volume $\tilde{v}$ due to the molecular mixing and diffusion and the chemical reactions in Eq. (3). Finally, $\dot{\omega}_v$ is a relaxation term defined as

$$\dot{\omega}_v = \overline{\rho}\frac{\tilde{v}_{PDF} - \tilde{v}}{\tau_v}, \qquad (6)$$

where $\tilde{v}_{PDF}$ is the Favre-averaged specific volume calculated in the Monte Carlo solver and τ_v is the relaxation time scale specified as $\tau_v = 4\Delta t$, where Δt is the time step used in the simulations. Then, the filtered density $\overline{\rho}$ is obtained as

$$\overline{\rho} = \frac{1}{\tilde{v}}. \qquad (7)$$

The simulations in this study are performed using the *pdfFoam*[38] solver developed entirely within OpenFOAM.[43]

B. Thermal boundary condition

The bluff-body wall is modeled as a fixed-temperature boundary in this study. A temperature profile that is measured experimentally by Euler *et al.*[44] is prescribed over the bluff-body surface. In the PDF solver, the heat loss is taken into account by adjusting the mean sensible enthalpy in the cells adjacent to the bluff-body surface. The mean
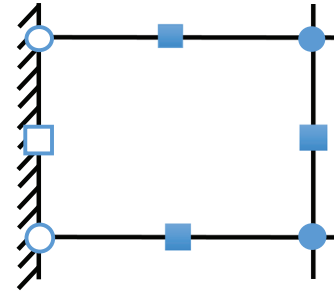

FIG. 1. The stencil of the computational cells adjacent to the bluff-body surface. The circles denote the cell vertices used to compute mean properties at particle locations, while the squares represent the face centers used to calculate the mean drift terms. The empty symbols denote the properties calculated using the experimental temperature profiles, while the filled symbols denote the properties obtained from the particles.

sensible enthalpy at the wall surface is calculated using the mean species mass fractions obtained from the particles and the measured wall temperature. After computing the mean sensible enthalpy at the wall, the sensible enthalpy of particles is updated according to mixing and transport that are calculated using the IEM mixing model and the mean drift term, as described in the particle composition equation [Eq. (3)]. Figure 1 shows the stencil used to interpolate mean properties onto the particle locations and to compute the mean drift terms in the boundary cells.

III. DETAILS OF THE BURNER AND COMPUTATIONAL SETUP

The Cambridge/Sandia burner was developed to study the effect of stratification in fuel concentration under both swirling and non-swirling conditions. In this study, we focus on the swirling conditions as the non-swirling cases have been studied previously.[25] The burner is shown in Fig. 2. The burner has a central bluff body and two annular fuel jets. An air coflow is provided at the outer part of the burner. The inner and outer fuel streams have bulk velocities of 8.31 m/s and 18.7 m/s, respectively. The outer fuel jet can provide swirling flows at different swirl numbers defined as the ratio of mean tangential velocity to the mean axial velocity ($S = U_{tg}/U_z$). In this study, only the cases with the swirl number of 0.79 are studied numerically. The bulk velocity of the air coflow is 0.4 m/s. The stratification ratio is defined as the ratio of the equivalence ratios at the inner and outer jets ($\phi_{inner}/\phi_{outer}$). The ratios for pure premixed (SwB3) and stratified cases (SwB7 and SwB11) are presented in Table I. The case of SwB7 referred to as the moderately stratified case has a ratio of 2, whereas the case of SwB11 referred to as the highly stratified case has a ratio of 3. Zhou *et al.*[45] made the measurements of the velocity data, and Sweeney *et al.*[19,20] made the measurements for the mass fraction of species and temperature.

The computational domain is selected as a cylindrical domain having dimensions of $L_x \times L_r \times L_\theta = 300 \text{ mm} \times 200 \text{ mm} \times 2\pi$ in the axial, radial, and azimuthal directions, respectively. A non-uniform structured grid of $256 \times 128 \times 96$ shown in Fig. 2 is used to discretize the domain. The grid is stretched close to the fuel exits in the axial direction and in the shear layers in the radial direction.
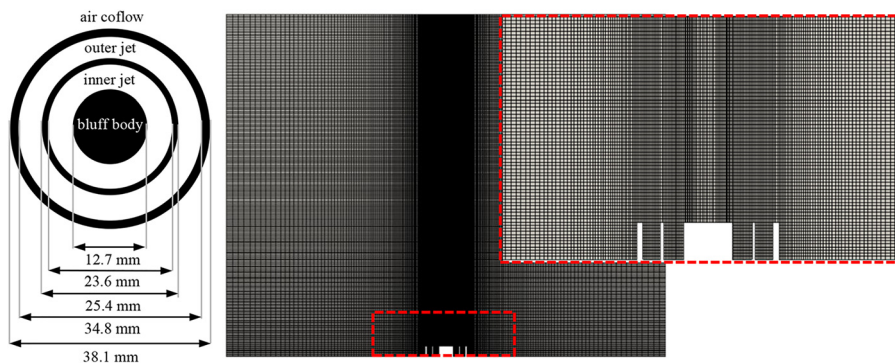
FIG. 2. The dimensions of the burner (left) and the computational mesh used in the simulations (right).

The instantaneous inlet velocities at the fuel inlets are obtained from two auxiliary turbulent non-swirling and swirling annular periodic pipe simulations for the inner and outer jets, respectively. In the pipe flow simulations, the axial and tangential velocities are corrected at each time step against the effect of numerical diffusion. A laminar bulk velocity of 0.4 m/s is applied at the air coflow inlet. At the bluff body and wall-lips, the no-slip boundary conditions are specified. At the surface of the bluff body, the experimental temperature profiles[44] are applied, the details of which will be given in Sec. II B. At the outlet and at the far field, the zero-gradient boundary conditions are used.

In the PDF solver, the nominal number of Lagrangian particles in each cell is kept around 20 by using a particle control algorithm. The mixing model parameter, C_m, is selected as $C_m = 25$. An augmented reduced mechanism (ARM1)[46] is used for methane/air combustion. Acceleration of chemical calculations is achieved by employing *in situ* adaptive tabulation (ISAT)[47,48] with an error tolerance of ϵ_{tol} of 5×10^{-5} as used in the previous studies.[25,36,49] The simulations are parallelized using a domain decomposition method[38] and performed using 192 cores. The time step in the simulations is selected as $\Delta t = 4 \times 10^{-6}$ s, resulting in a Courant number of around 0.2. The simulations are first calculated for 15 flow-through times to reach a statistically stationary state, and then, additional ten flow-through times are run to collect the statistics.

The parametric models investigated in this study are defined in Table II. The non-adiabatic boundary conditions described in Sec. II B are applied in model DD-HL (baseline), while the adiabatic boundary conditions are used in models DD-AD and ED-AD. The differential diffusion effect is included in models DD-HL and DD-AD, while the unity Lewis number approximation is used for all species in model ED-AD. Here, we note that the DD model accounts for the differential diffusion only in the molecular transport term [the second term on the RHS of Eq. (3)], while the unity Lewis number approximation is applied in the molecular mixing term [the first term on the RHS of Eq. (3)]. The effect of heat loss from the bluff body is examined by

comparing models DD-HL and DD-AD. The effects of the differential diffusion are assessed and quantified by comparing models DD-AD and ED-AD.

IV. RESULTS

In this section, the numerical results for the baseline model are first presented by comparing with the experimental measurements, including the general behaviors in Sec. IV A, the mean and rms velocities in Sec. IV B, the mean and rms scalars in Sec. IV C, and the scatter plots of species in Sec. IV D. Following the detailed comparison, the effect of stratification on the flame structure under swirling conditions is presented and discussed. The effect of differential diffusion and the effect of heat loss from the bluff body are discussed in Secs. IV E and IV F, respectively.

A. The general characteristics of the flames

The contour plots of the mean axial velocity with the mean streamlines, the mean temperature, and the mean equivalence ratio from model DD-HL are presented in Fig. 3. The recirculation zones are calculated approximately as 100 mm long for all the cases. We note that the experimental velocity data are only available until the axial location of $z = 65$ mm, which is within the recirculation zone in swirling conditions. Therefore, the length of the recirculation zone is not available experimentally. Note that the lengths of the recirculation zone under the non-swirling condition have been calculated in the companion paper[25] as 23 mm, 13.5 mm, and 14 mm for the premixed (SwB1), the moderately (SwB5), and the highly (SwB9) stratified cases, respectively. These results demonstrate the strong influence of swirl on the length and overall flow structure of the recirculation zone. Note that the effects of reaction on the length of the recirculation zone have been recently examined by Massey *et al.*,[50] but they considered only the non-swirling cases. Based on the model developed for the non-swirling cases, they predicted that swirl shortens the length of the recirculation zone, which is in contrast with the experimental and

TABLE I. Equivalence ratios at the fuel jets.

Case	ϕ_{inner}	ϕ_{outer}	$\phi_{inner}/\phi_{outer}$
SwB3	0.75	0.75	1
SwB7	1	0.5	2
SwB11	1.125	0.375	3

TABLE II. Model variations for parametric studies.

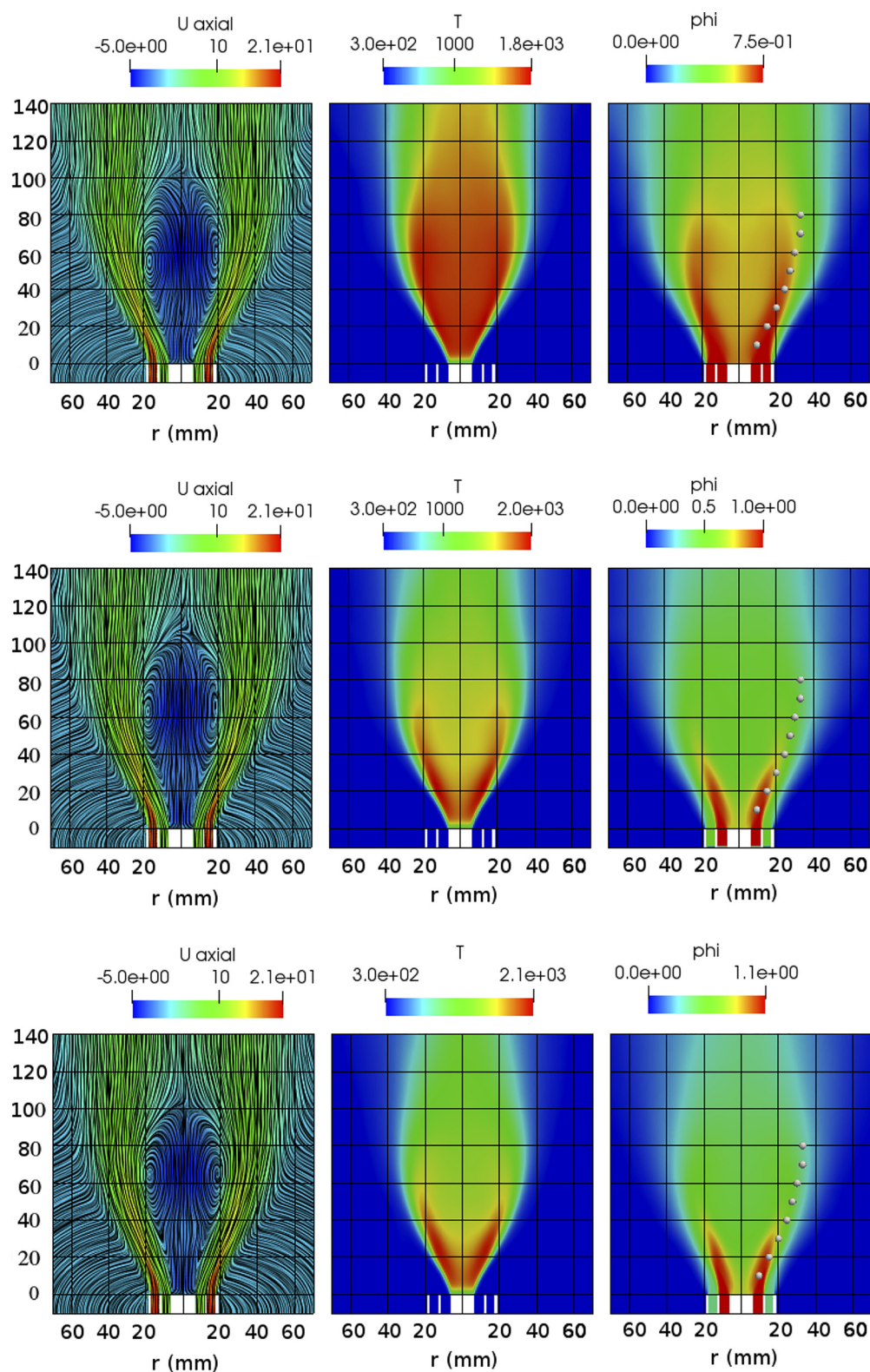| Model	Differential diffusion	Heat loss
DD-AD	✓	✗
DD-HL	✓	✓
ED-AD	✗	✗

FIG. 3. The mean axial velocity with the mean streamlines (left), the mean temperature (middle), and the mean equivalence ratio (right) from the simulations with model DD-HL. Rows 1–3: SwB3, SwB7, and SwB11.

numerical results obtained for the present flame series. A further investigation is required for the effects of swirl on the length and flow structure of the recirculation zone, which is not in the scope of the present paper.

The long recirculation zone brings the cold and low-equivalence ratio fluid from the downstream to the upstream positions, which reduces the temperature and equivalence ratio within the recirculation zone close to the centerline due to mixing. The level of reduction in temperature and equivalence ratios is higher in the stratified cases of SwB7 and SwB11 than those in the premixed case, SwB3. In the stratified cases, SwB7 and SwB11, at the axial location of 10 mm, the temperature and equivalence ratio at the centerline are ∼7% and 35%, respectively, lower than those in the vicinity of the flame front within the recirculation zone. In contrast with the premixed case (SwB3) at the same axial location in SwB3, the differences in temperature and equivalence ratio at the centerline and in the vicinity of the flame front within the recirculation zone are ∼1% and 17%, respectively.

The flame fronts, defined as the loci of the peak of the rms temperature in the radial direction, are depicted by the white points in Fig. 3. In SwB3, the flame front mainly propagates in a uniform equivalence ratio mixture. At ∼50 mm, the flame front starts to propagate in a mixture with slight gradients of equivalence ratio created by mixing between the fuel streams and the air coflow. For SwB7 and SwB11, the flame fronts encounter a stratified mixture after approximately $z = 20$ mm because of the different equivalence ratios streaming from the inner and outer jets.

The effect of the heat loss from the bluff body can be observed in the vicinity of the bluff-body surface. The temperature within this region is significantly reduced due to the heat loss effect, which will be further discussed in Sec. IV F.

B. Velocities

The mean and rms of the axial, radial, and tangential velocities are presented in this section for a detailed model assessment. First, to demonstrate the conformity of the computational and the experimental inlet boundary conditions, the mean and rms velocity profiles are plotted in Fig. 4 for the SwB3 case at the axial location of 2 mm, and the closest axial location to the jet exits where the experimental data are available. As seen, the mean and rms velocity profiles are in good agreement with the experimental data. Although not shown here due to space consideration, the computed velocity profiles are also found to be in good agreement with the experimental data at the same axial location for the SwB7 and SwB11 cases. The radial profiles calculated from SwB3, SwB7, and SwB11 at three different axial locations are presented together with the experimental measurements, as shown in Figs. 5–9. The mean axial velocities are in good agreement with the experimental measurements. Slight discrepancies are observed close to the centerline at the downstream locations in SwB7 and SwB11. The mean tangential velocities also agree well with the experimental measurements, as shown in Fig. 6. However, the peak values are over-predicted by ∼10% at $z = 10$ mm. The mean radial velocities demonstrate good consistency with the experimental data for all three cases, as shown in Fig. 7. Deviations are more obvious at the downstream locations. The peak values are over-predicted by less than 10%, and the profiles are slightly shifted outward from the centerline, indicating that stronger expansion toward the radial direction due to the swirling flow is predicted by all three model combinations.

The profiles of the rms of the axial, tangential, and radial velocities agree well with the experimental data for all three cases, as shown in Figs. 8 and 9. As shown in Fig. 8, the peaks of the rms axial velocity
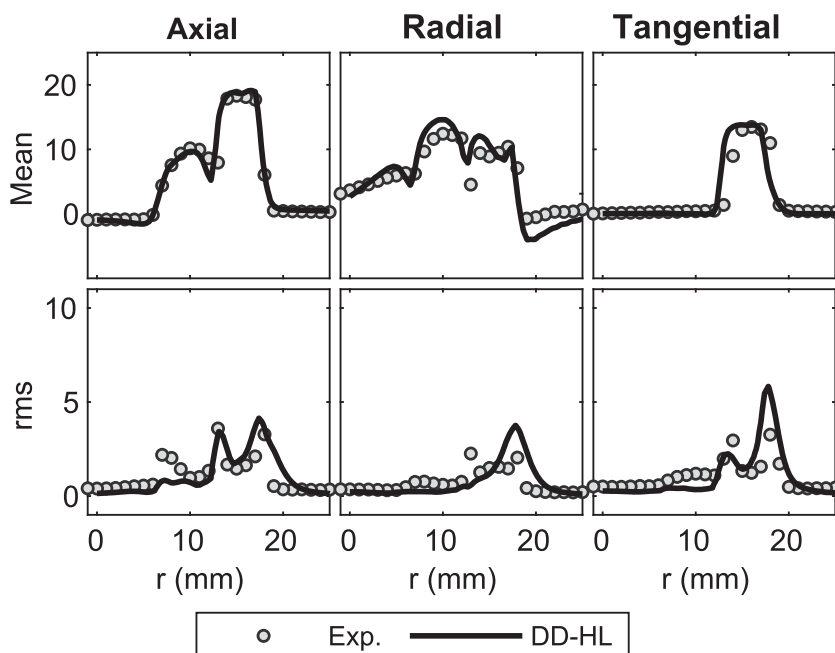
FIG. 4. The mean and rms velocity profiles at $z = 2$ mm. Symbols: the measurements; red line: model DD-HL.
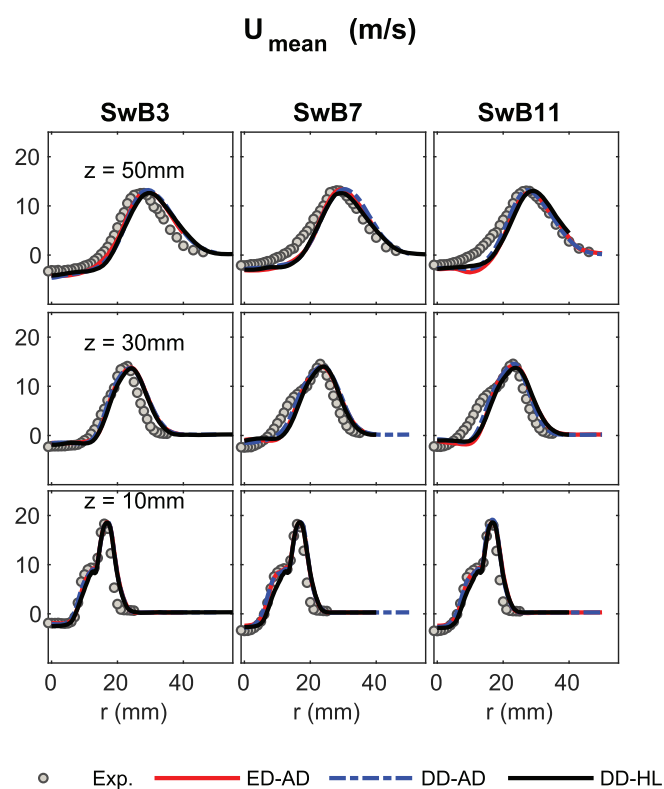
U_{mean} (m/s)

FIG. 5. Results of the time-averaged axial velocity at 10 mm, 30 mm, and 50 mm distance from the fuel jet exits (from bottom to top). Symbols: the measurements; red line: model ED-AD; blue dashed line: model DD-AD; black line: model DD-HL.
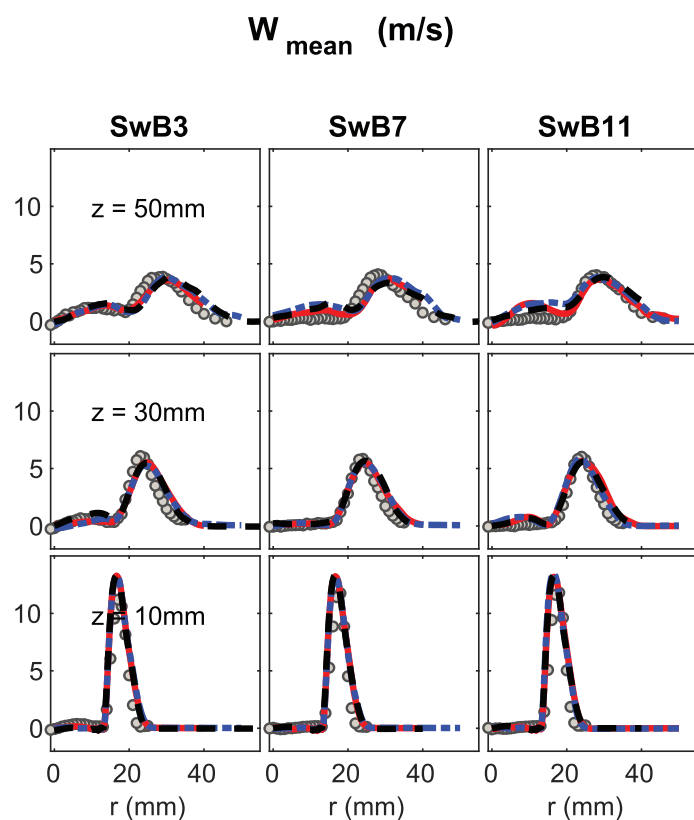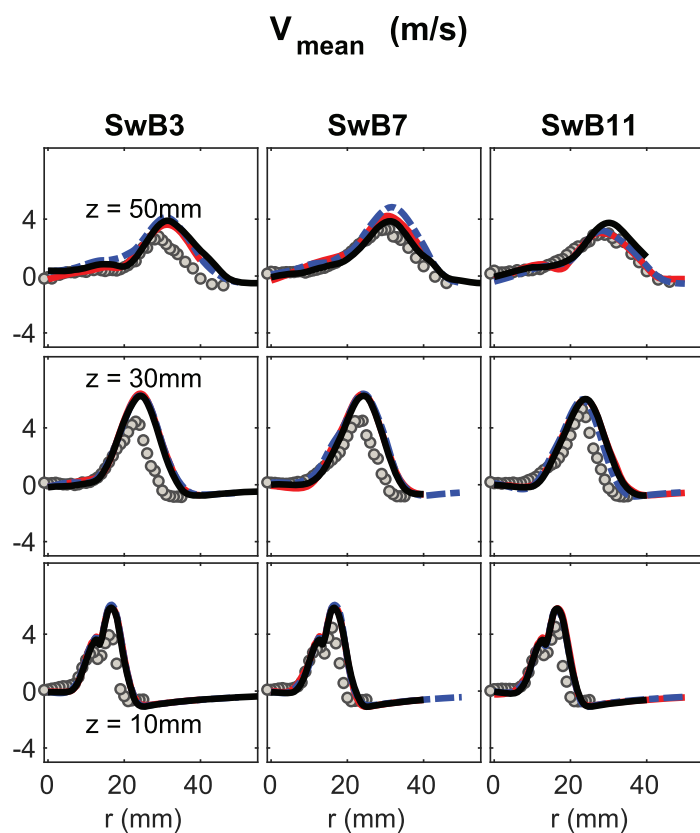
W_{mean} (m/s)

FIG. 6. Results of the time-averaged tangential velocity at 10 mm, 30 mm, and 50 mm distance from the fuel jet exits (from bottom to top). Symbols: the measurements; red line: model ED-AD; blue dashed line: model DD-AD; black line: model DD-HL.
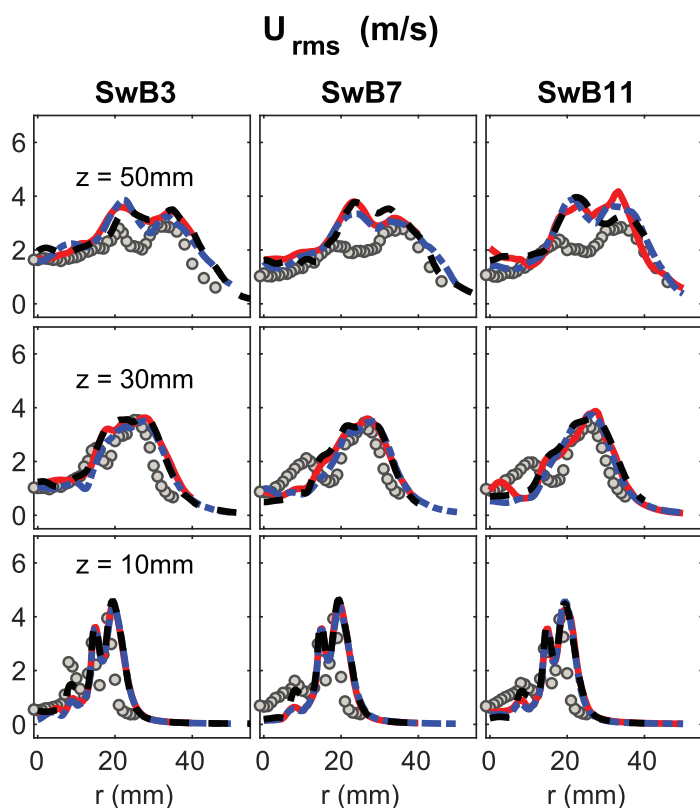
FIG. 7. Results of the time-averaged radial velocity at 10 mm, 30 mm, and 50 mm distance from the fuel jet exits (from bottom to top). Symbols: the measurements; red line: model ED-AD; blue dashed line: model DD-AD; black line: model DD-HL.
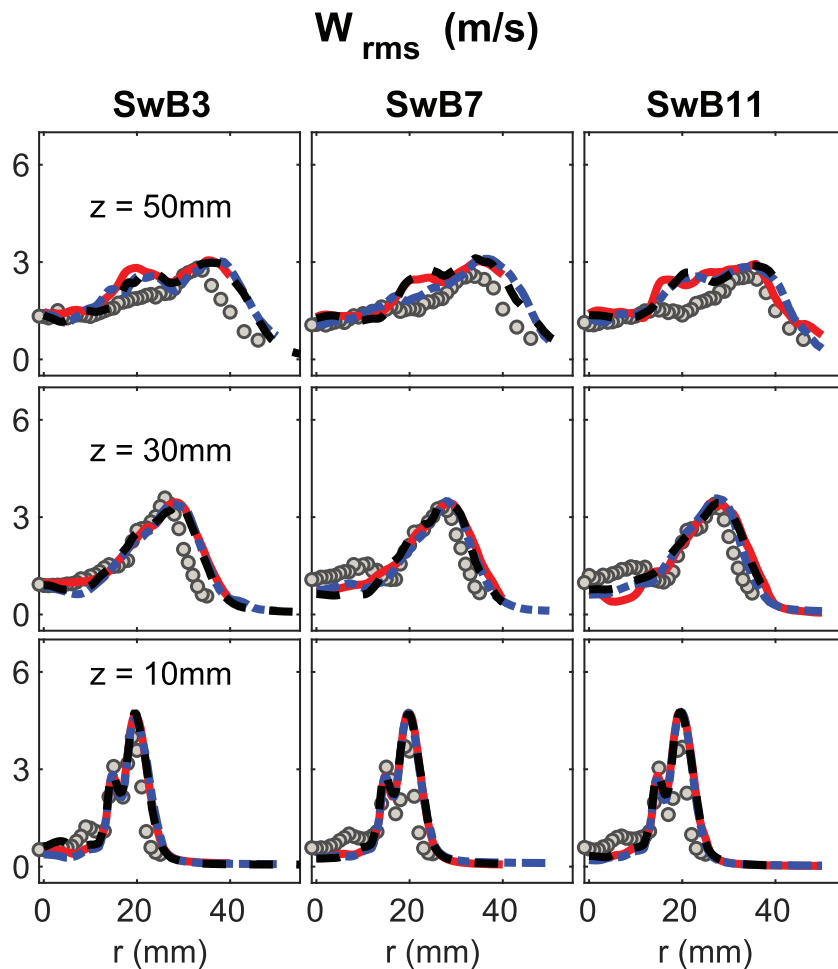

FIG. 8. Results of the rms of the axial velocity at 10 mm, 30 mm, and 50 mm distance from the fuel jet exits (from bottom to top). Symbols: the measurements; red line: model ED-AD; blue dashed line: model DD-AD; black line: model DD-HL.

FIG. 9. Results of the rms of the tangential velocity at 10 mm, 30 mm, and 50 mm distance from the fuel jet exits (from bottom to top). Symbols: the measurements; red line: model ED-AD; blue dashed line: model DD-AD; black line: model DD-HL.

are over-predicted at $z = 50$ mm within the recirculation zone, and the over-prediction is more prominent in the stratified cases. The over-prediction of fluctuating velocity might be caused by the under-prediction of temperature within the recirculation zone, which will be further discussed in Sec. IV C. The rms radial velocity profiles in Fig. 10 are slightly shifted outward, which is consistent with the observed shift in the mean radial velocity profiles in Fig. 7.

C. Scalars

In this section, the numerical results for scalar profiles of the mean temperature T, equivalence ratio ϕ, and mass fractions of CH_4, CO_2, O_2, and CO are presented and compared with the experimental data at four axial locations in Figs. 11–13. The mean temperatures are overall in good agreement with the measurements for all the cases. The mean temperature at $z = 10$ mm is overestimated by ~ 100 K by model DD-HL for all the cases. Further downstream at 50 mm and 60 mm, the mean temperatures for SwB3 are well estimated, whereas the peak values of the temperature profiles are under-predicted by ~ 200 K for SwB7 and SwB11 at the same locations. As observed in Fig. 3, the center of the recirculation zones is located approximately at

$z = 60$ mm for all the cases. The strength of the recirculating flow field can have strong effects on the temperature profiles at those locations. Therefore, the discrepancies of temperature at $z = 50$ mm and $z = 60$ mm can be attributed to the discrepancies in the prediction of the recirculating zone.

The equivalence ratio results demonstrate the overall good agreement with the measurements for all three cases. At downstream locations of 30 mm, 50 mm, and 70 mm, the equivalence ratio profiles are underestimated in SwB7 and SwB11. The under-predicted equivalence ratios inside the recirculation zones are consistent with the observed under-prediction of temperature at the same locations and may result from the strong effect of mixing with downstream airs within the recirculation zone.

The mean CH_4 results exhibit a good agreement with the measurements for all three cases. The CO_2 and O_2 results are well estimated in the premixed case of SwB3. In SwB7 and SwB11, the CO_2 and O_2 results are in good agreement with the experiment at the axial location of 10 mm; however, the CO_2 concentration is slightly underestimated and the O_2 concentration is slightly overestimated inside the recirculation zone close to the flame front (approximately $r = 25$ mm in Fig. 3) at $z = 50$ mm and 60 mm. For SwB3, the profiles of CO are
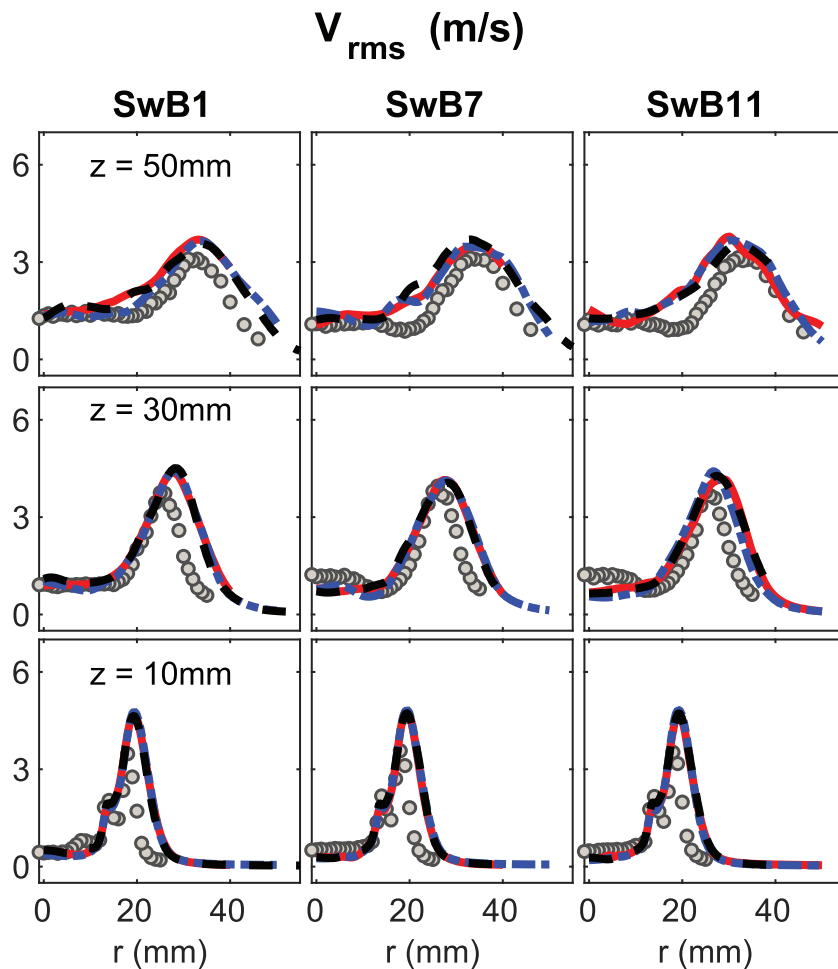
FIG. 10. Results of the rms of the radial velocity at 10 mm, 30 mm, and 50 mm distance from the fuel jet exits (from bottom to top). Symbols: the measurements; red line: model ED-AD; blue dashed line: model DD-AD; black line: model DD-HL.

well predicted at all the axial locations. The peak values of the CO profiles are in very good agreement with the experiment at $z = 10$ mm, while they are slightly underestimated at the downstream locations. For the cases of SwB7 and SwB11, the profiles of CO are well predicted at $z = 10$ mm, while the CO profile is underpredicted at the downstream locations.

Finally, the total rms of temperature, equivalence ratio, and mass fractions of species are compared with the measurements in Figs. 14–16. All the profiles are overall in good agreement with the measurements. At downstream locations, the rms results are lower than the measurements; however, the trends in the numerical results are in good agreement with the experimental measurements. The rms of the equivalence ratio, O_2, CO_2, and CO is underestimated at $z = 50$ mm and 60 mm for all three cases.

D. Scatter plots

In this section, the scatter plots generated using the notional Lagrangian particles are presented for the mole fractions of species, CO_2, H_2, CO, CH_4, H_2O, O_2, and the equivalence ratio, ϕ, in the

temperature space at $z = 10$ mm together with the experimental scattered data in Figs. 17–19. The mean values, $\langle X_\alpha | T \rangle$ (conditioned on temperature), are also presented by comparing with the experimental data. The figures are colored by the equivalence ratio. The scatter plots from the numerical simulations exhibit a close agreement with the experimental data. The distribution of the scatter plots from the simulations cover a narrower region in the temperature space than those in the experimental measurements, which is similar to the one observed in the simulations under the non-swirling condition.[25]

The experimental data points extend to smaller values in the equivalence ratio space than those obtained from the numerical simulations, particularly for $T > 1500$ K. For the premixed case of SwB3, the lowest equivalence ratio is smaller than the value at the fuel jets, suggesting entrainment of downstream air and/or diluted mixture deep into the recirculation zone. The lowest equivalence ratios observed in the cases of SwB7 and SwB11 above $T = 1500$ K also result from the same entrainment mechanism.

The conditional means of species from the LES/PDF simulations are overall in close agreement with the experimental scatter data for temperature lower than 1500 K. However, considerable discrepancies
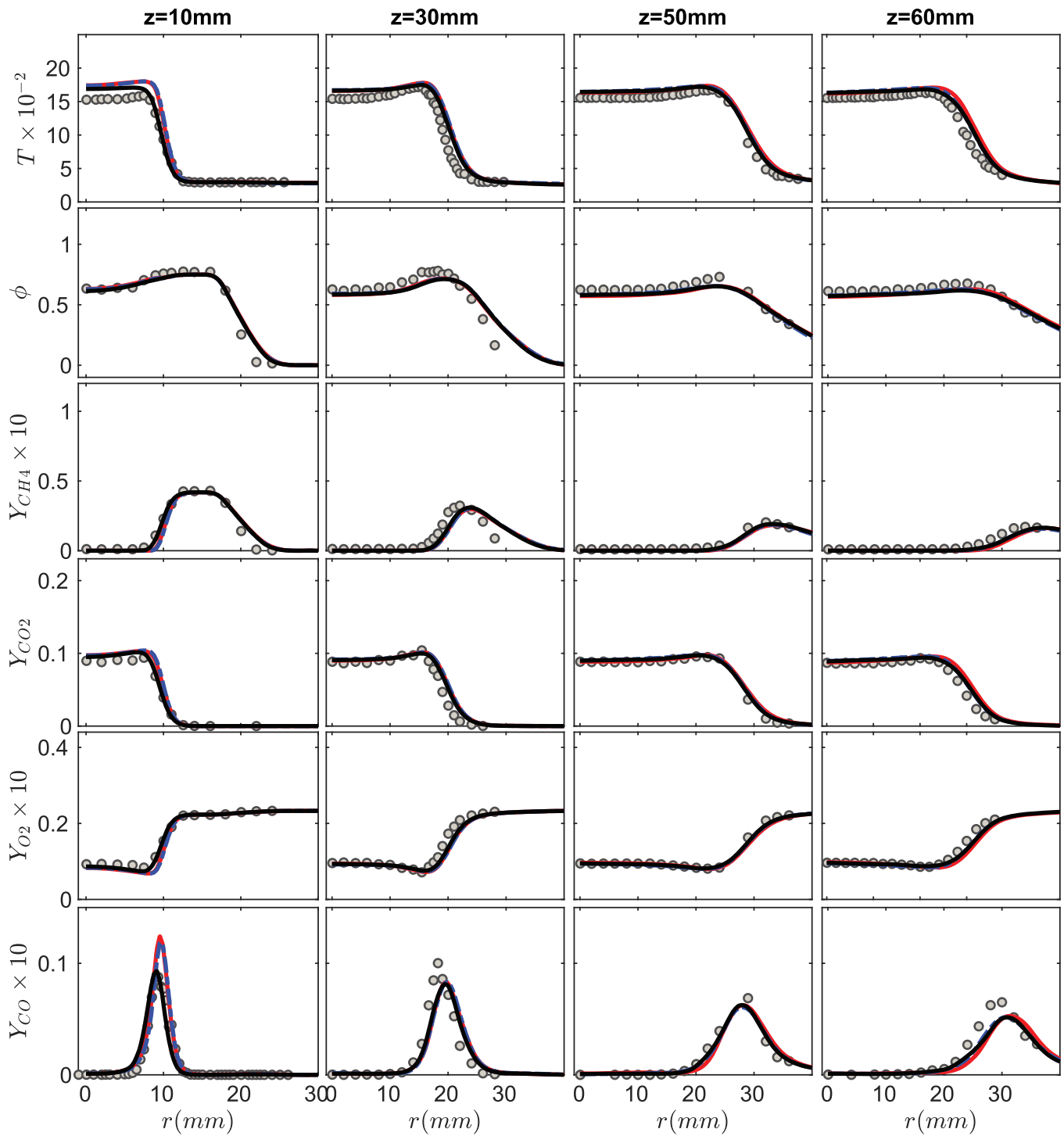
SwB3 Mean

FIG. 11. SwB3: The mean temperature and mass fractions of CH$_4$, CO$_2$, O$_2$, and CO (from top to bottom) at axial locations of $z = 10$ mm, 30 mm, 50 mm, 60 mm (from left to right). Symbols: the measurements; red line: model ED-AD; blue dashed line: model DD-AD; black line: model DD-HL.
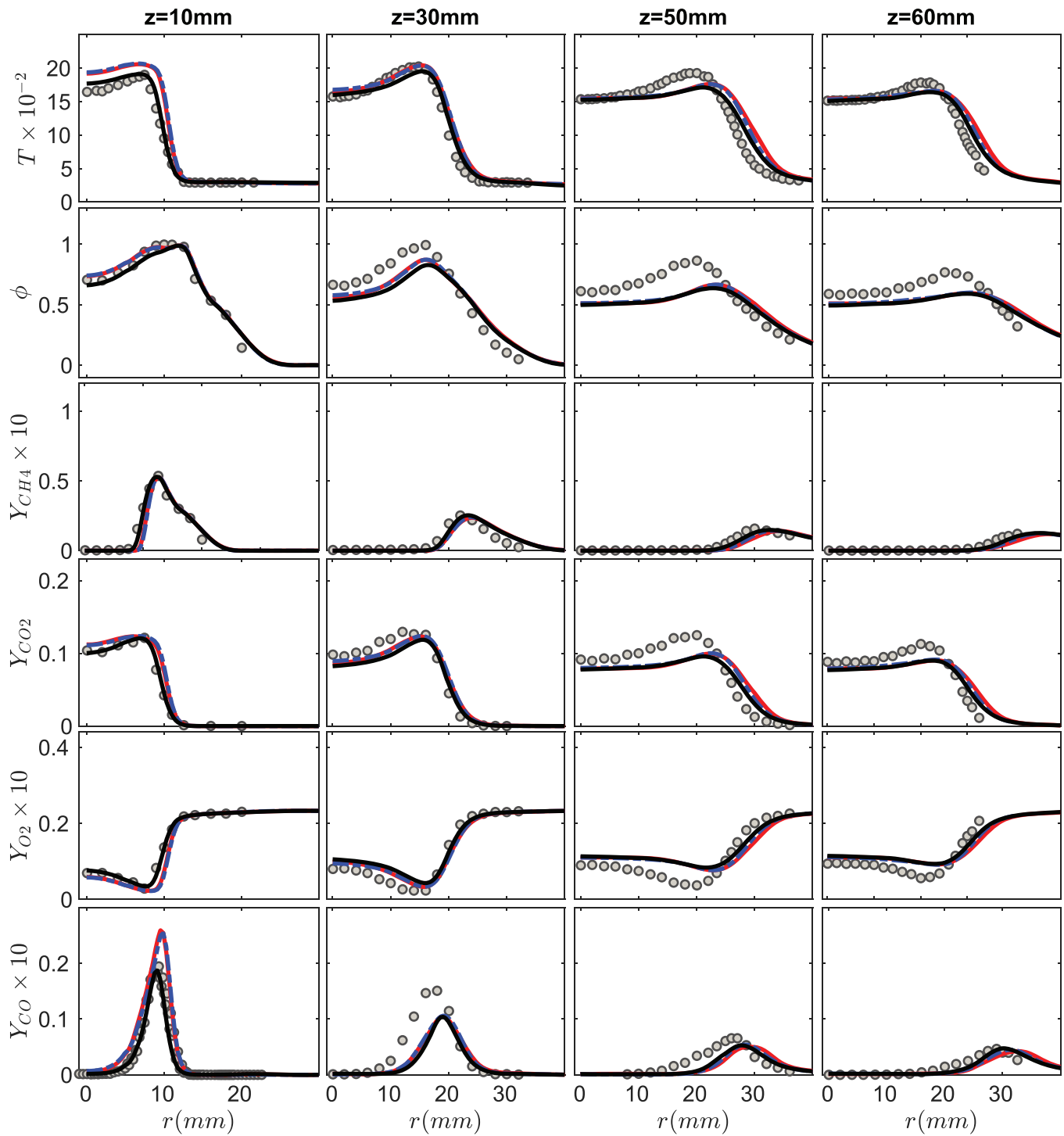
SwB7 Mean

FIG. 12. SwB7: the mean temperature and mass fractions of CH_4, CO_2, O_2, and CO (from top to bottom) at axial locations of $z = 10$ mm, 30 mm, 50 mm, 60 mm (from left to right). Symbols: the measurements; red line: model ED-AD; blue dashed line: model DD-AD; black line: model DD-HL.
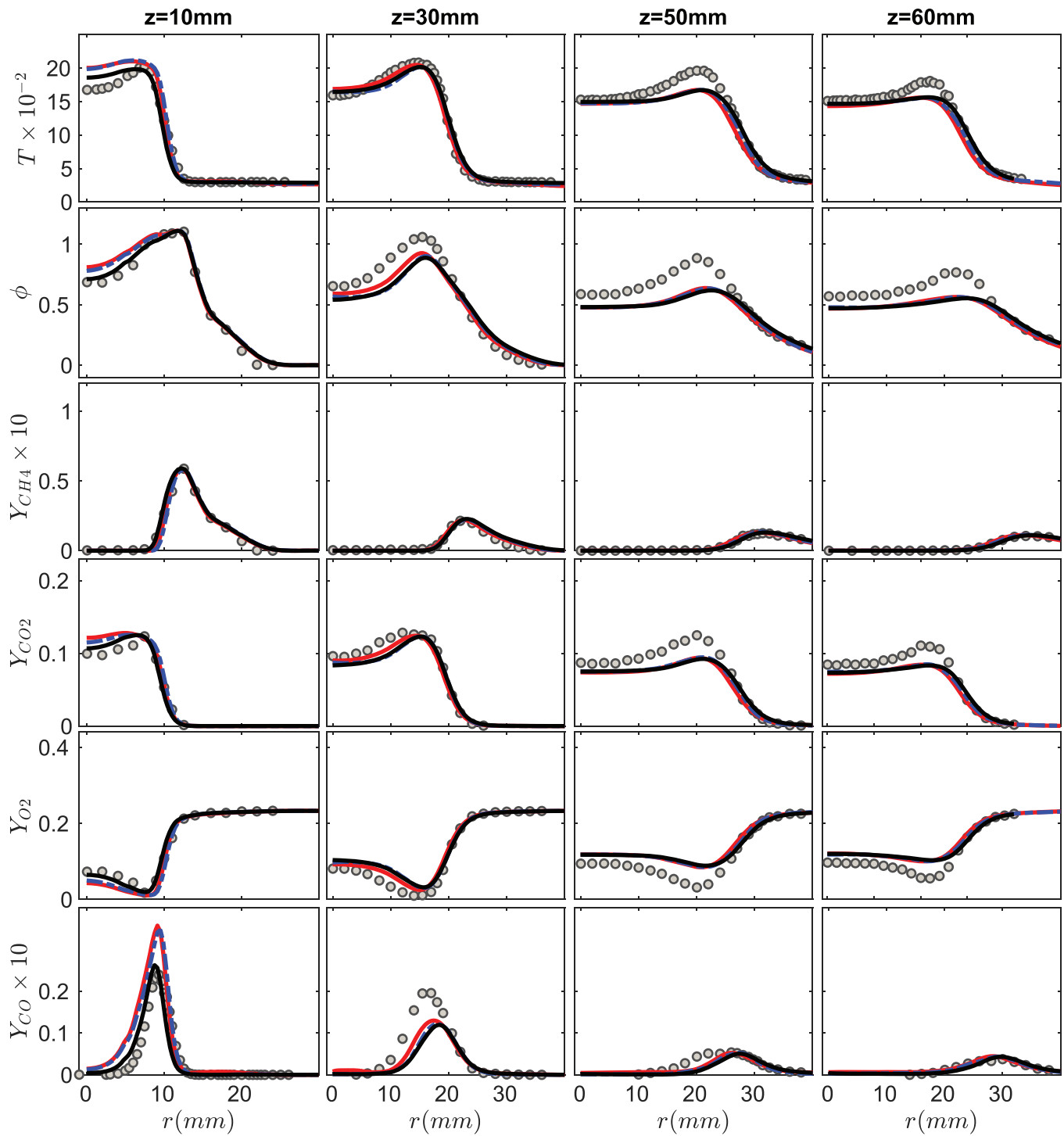
SwB11 Mean

FIG. 13. SwB11: the mean temperature and mass fractions of CH_4, CO_2, O_2, and CO (from top to bottom) at axial locations of $z = 10$ mm, 30 mm, 50 mm, 60 mm (from left to right). Symbols: the measurements; red line: model ED-AD; blue dashed line: model DD-AD; black line: model DD-HL.
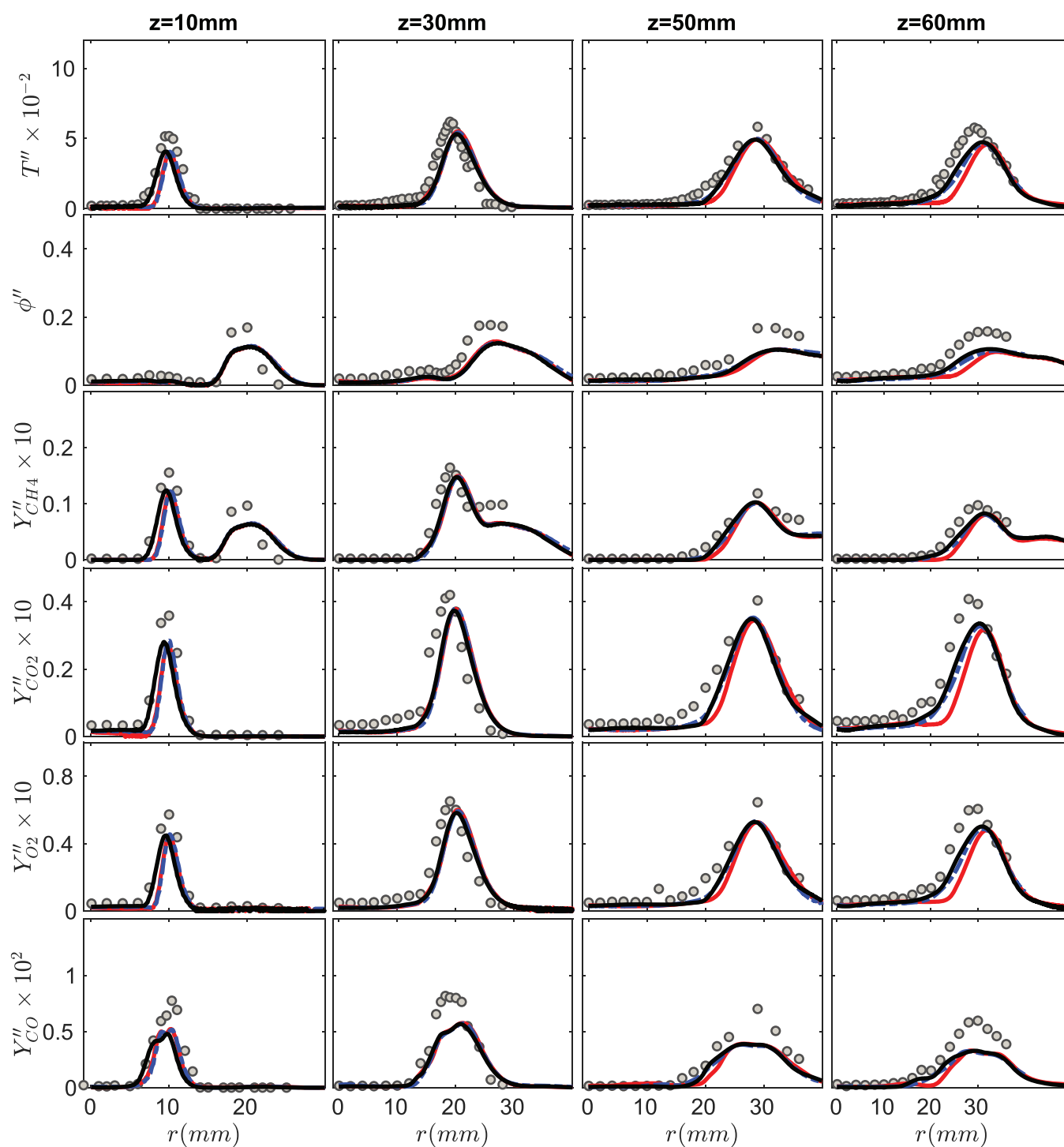
SwB3 RMS

FIG. 14. SwB3: the rms temperature and mass fractions of CH$_4$, CO$_2$, O$_2$, and CO (from top to bottom) at axial locations of $z = 10$ mm, 30 mm, 50 mm, 60 mm (from left to right). Symbols: the measurements; red line: model ED-AD; blue dashed line: model DD-AD; black line: model DD-HL.

FIG. 15. SwB7: the rms temperature and mass fractions of CH$_4$, CO$_2$, O$_2$, and CO (from top to bottom) at axial locations of $z = 10$ mm, 30 mm, 50 mm, 60 mm (from left to right). Symbols: the measurements; red line: model ED-AD; blue dashed line: model DD-AD; black line: model DD-HL.
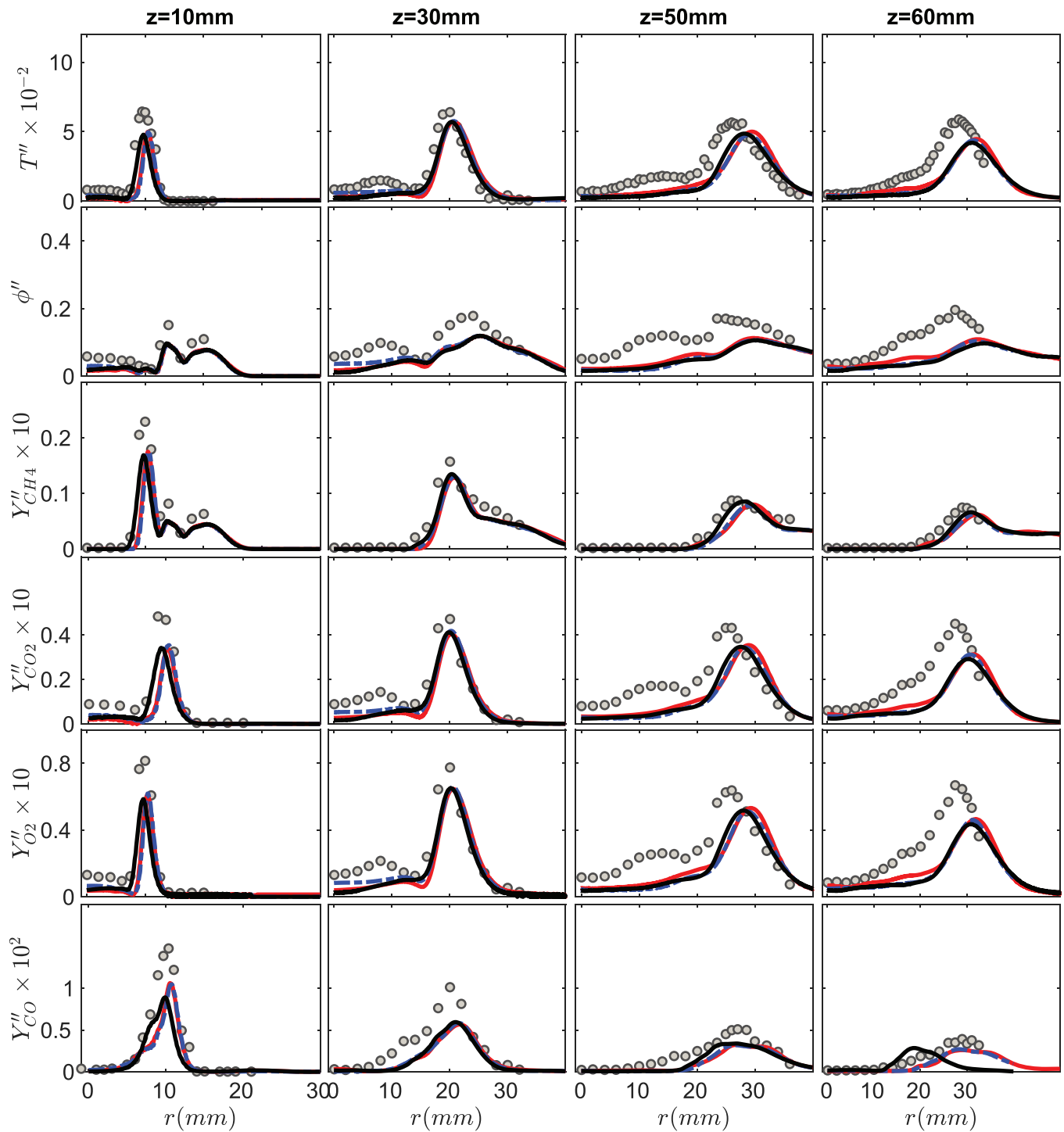
SwB11 RMS

FIG. 16. SwB11: the rms temperature and mass fractions of CH_4, CO_2, O_2, and CO (from top to bottom) at axial locations of $z = 10\,mm$, $30\,mm$, $50\,mm$, $60\,mm$ (from left to right). Symbols: the measurements; red line: model ED-AD; blue dashed line: model DD-AD; black line: model DD-HL.
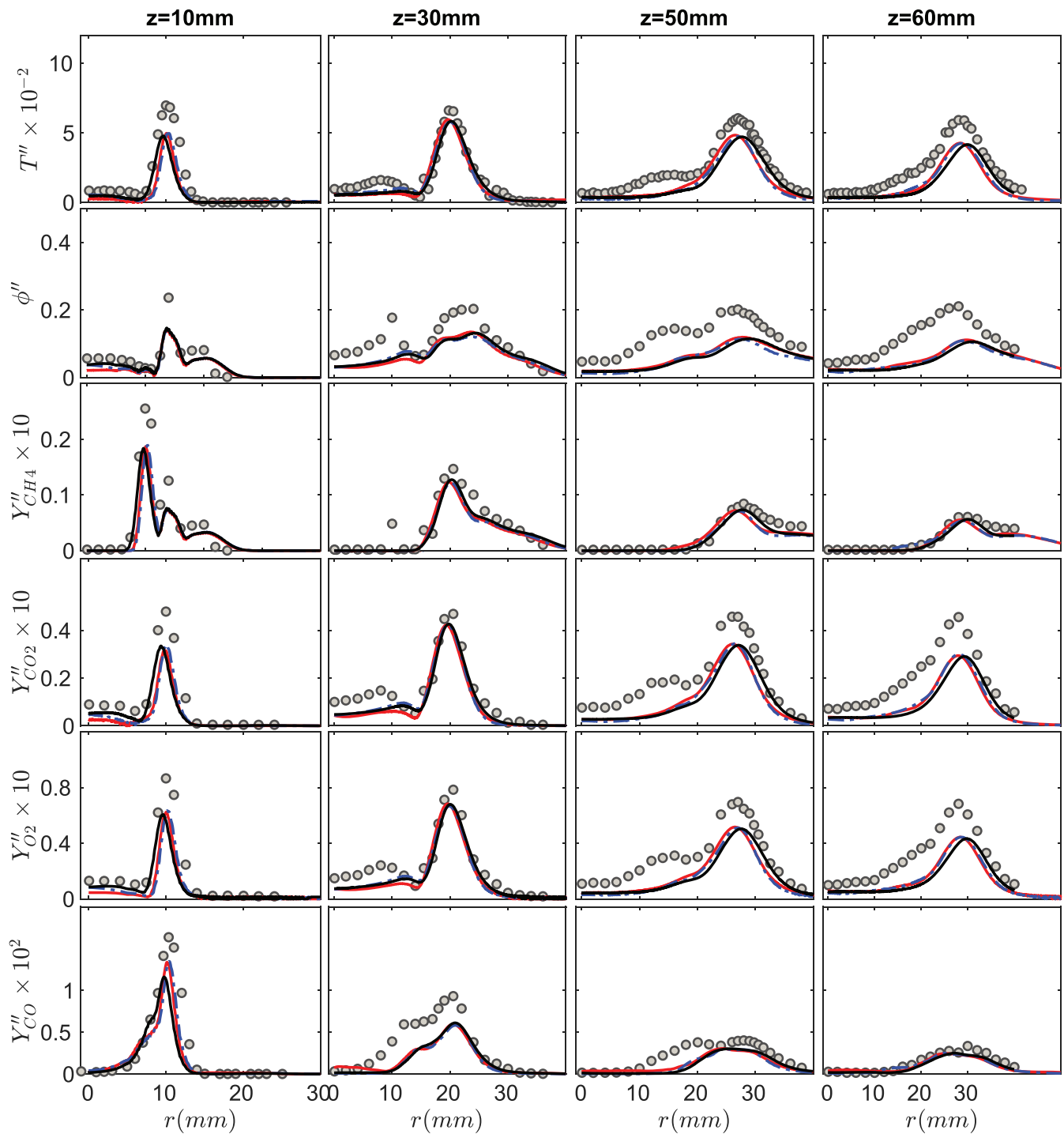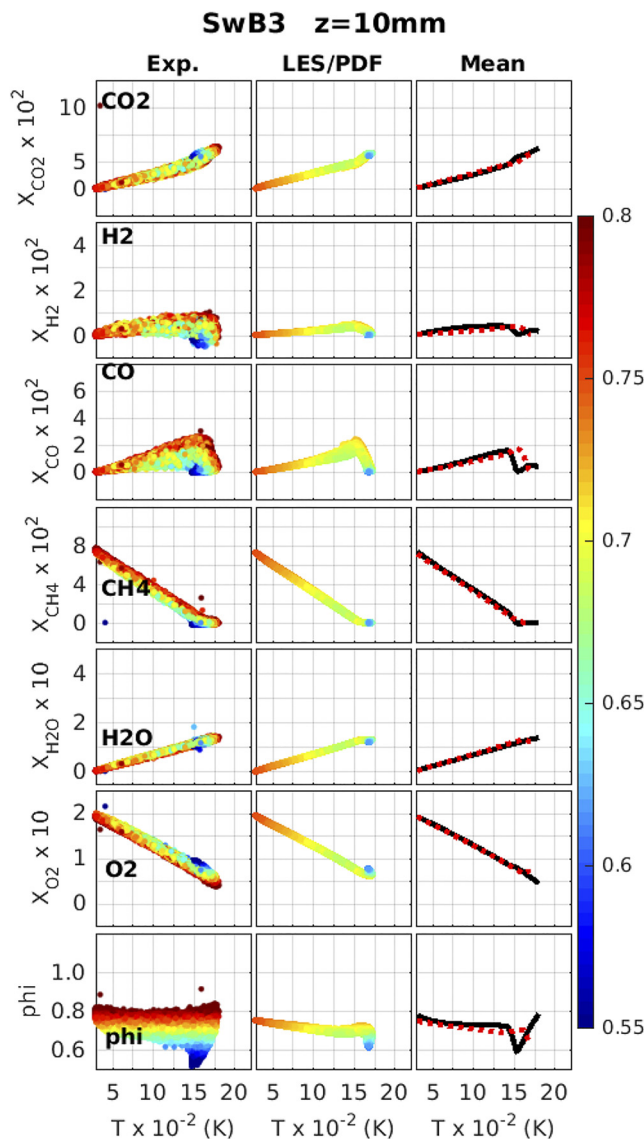
FIG. 17. SwB3: scatter plots of mole fractions of species of CO_2, H_2, CO, CH_4, H_2O, O_2, and ϕ in temperature space from the numerical simulations and the experimental data at $z = 10$ mm, colored with the equivalence ratio. Black solid line: the conditional mean (conditioned on temperature) of species mole fractions from the experiment; red dashed line: conditional mean (conditioned on temperature) of species mole fractions from the simulation.

FIG. 18. SwB7: scatter plots of mole fractions of species of CO_2, H_2, CO, CH_4, H_2O, O_2, and ϕ in temperature space from the numerical simulations and the experimental data at $z = 10$ mm, colored with the equivalence ratio. Black solid line: the conditional mean (conditioned on temperature) of species mole fractions from the experiment; red dashed line: conditional mean (conditioned on temperature) of species mole fractions from the simulation.

are observed between the conditional means from the experimental and the numerical results for temperatures higher than 1500 K mainly because the simulations over-predict the equivalence ratio at these temperatures.

To further understand the physical locations where the discrepancy in the conditional means originates, the scatter plots of CO mass fraction in temperature space at $z = 10$ mm are presented in Fig. 20. Here, the scattered data are colored by the radial positions of the
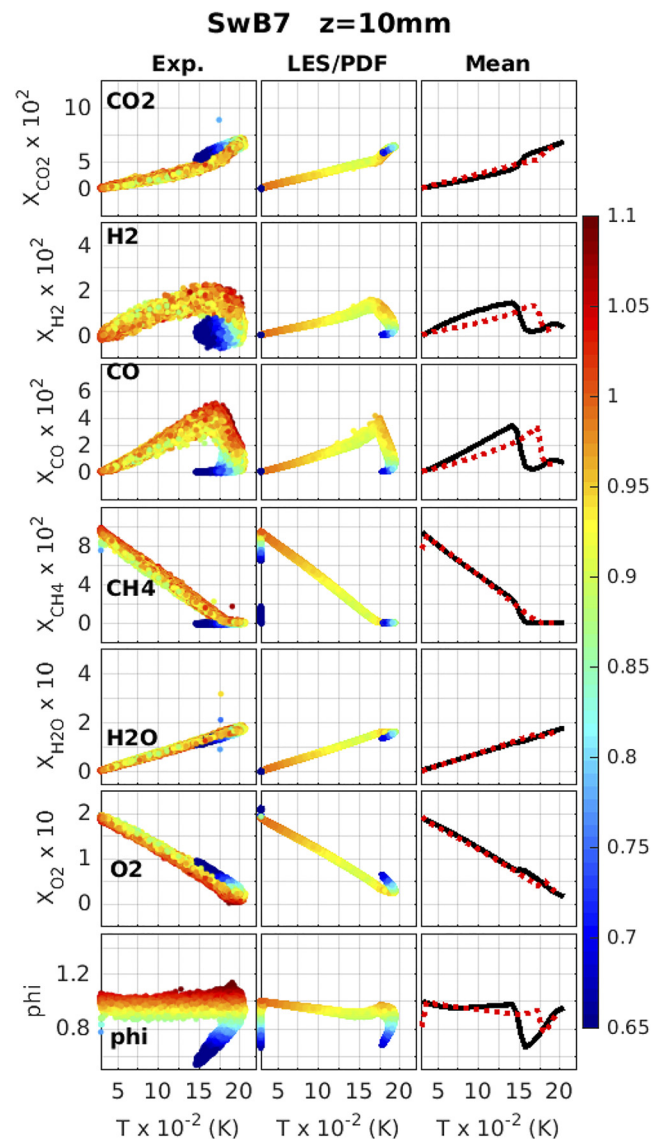
Lagrangian particles. Furthermore, the color of points located within the 5 mm distance from the centerline is marked as black to demonstrate the behavior of the CO distribution close to the centerline. As observed in Fig. 20, the points with low equivalence ratios are located closed to the centerline. Considering the recirculating flow fields given in Fig. 3, the points close to the centerline mainly are entrained from the locations with lower equivalence ratio downstream. Therefore, accurate prediction of the recirculation region is important for correct
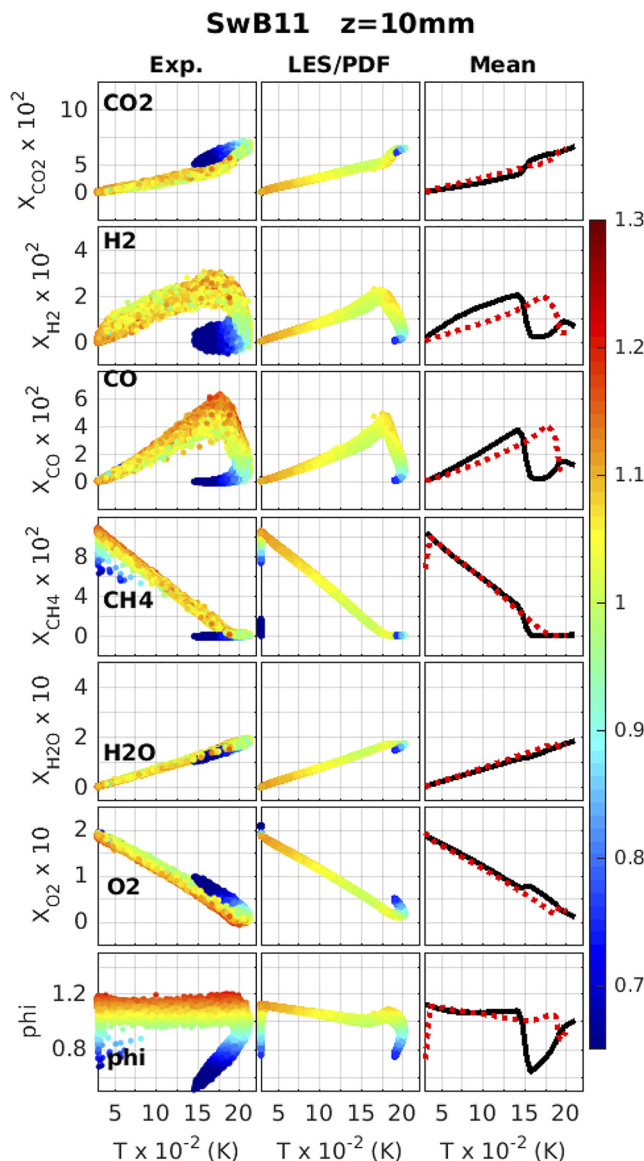
FIG. 19. SwB11: scatter plots of mole fractions of species of CO_2, H_2, CO, CH_4, H_2O, O_2, and ϕ in temperature space from the numerical simulations and the experimental data at $z = 10$ mm, colored with the equivalence ratio. Black solid line: the conditional mean (conditioned on temperature) of species mole fractions from the experiment; red dashed line: conditional mean (conditioned on temperature) of species mole fractions from the simulation.

prediction of the scalars. Compared to the shorter recirculation region observed in Ref. 25, the cases with swirling flow in this study are more challenging computationally. The extent of the computational domain and the outlet boundary conditions can potentially impact the states within the recirculation zone, which subsequently impact the flame stabilization. Although not shown in this paper due to space consideration, the scatter plots at further downstream locations have similar

agreement with the experimental data as also observed for the non-swirling case studied by Turkeri *et al.*[25]

E. Effect of differential diffusion

The effect of differential diffusion is studied by examining the results obtained from models DD-AD and ED-AD. It should be emphasized that only the resolved molecular differential diffusion is considered by the models employed here. The mean and the rms velocity as well as the scalar fields from models DD-AD and ED-AD are very similar for SwB3, SwB7, and SwB11, as demonstrated in Figs. 5–13. Therefore, the resolved molecular differential diffusion is found to have insignificant impact on the mean velocity and scalar fields under the swirling conditions. This is in contrast with the non-swirling conditions, where the differential diffusion has been found to slightly modify the velocity profiles by shortening the recirculation zone behind the bluff body.[25] When the recirculation zone is created by both the bluff body and the swirling flow, the differential diffusion seems to play a secondary role in affecting the size of the recirculation zone compared to the non-swirling conditions.

F. Effect of heat loss from the bluff body

Finally, the effect of heat loss from the bluff body is studied by comparing the results obtained from models DD-HL and DD-AD. The mean and the rms velocity profiles from the two models are very similar to one another, as shown in Figs. 5–16, which indicates that the heat loss has a negligible effect on the velocity profiles. The temperature profiles from model DD-HL are in better agreement with the experimental data than those from model DD-AD at $z = 10$ mm for all the cases. Model DD-HL over-predicts the mean temperature by $\sim$100 K, while model DD-AD over-predicts by $\sim$300 K close to the centerline in SWB7 and SwB11 at $z = 10$ mm.

The mean CO profiles from model DD-HL are in very good agreement with the experimental measurements, while model DD-AD over-predicts CO mass fractions by $\sim$25% at $z = 10$ mm. This is mainly due to the higher temperature predicted by model DD-AD.

The mean equivalence ratio profiles from models DD-HL and DD-AD are very similar in the premixed case, SwB3. For the moderately stratified case SwB7, model DD-HL produces slightly lower profiles than those from model DD-AD at $z = 10$ mm. For the highly stratified case, SwB11, the result from model DD-HL is in better agreement with the measurements than those from model DD-AD at $z = 10$ mm, while model DD-AD predicts the equivalence ratio 5% higher than the measurements at that axial location.

The mean mass fraction of CH_4, CO_2, and O_2 from model DD-HL are in slightly better agreement with the measurements than those from model DD-AD within the recirculation zone ($r < 12$ mm) at $z = 10$ mm. Comparing to CO, mass fractions of CH_4, CO_2, and O_2 demonstrate lower levels of sensitivity to the heat loss effect.

For all the scalar profiles, models DD-HL and DD-AD predict very similar results at further downstream locations of $z = 30$ mm, 50 mm, and 70 mm, which indicates a negligible effect of heat loss at these locations. The rms profiles of temperature, equivalence ratio, and mass fractions of CH_4, CO_2, O_2, and CO from models DD-HL and DD-AD are also very close to one another at all the axial locations.
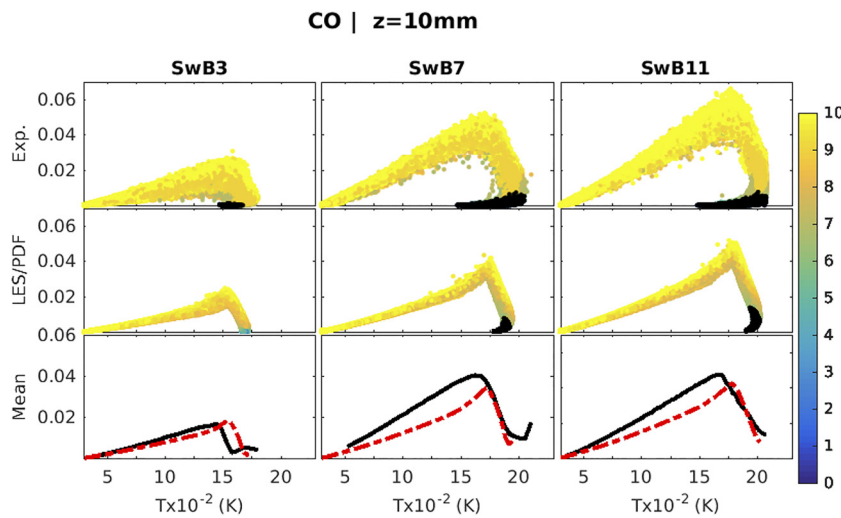
CO | z=10mm

FIG. 20. Scatter plots of mass fractions of CO in temperature space from the experimental data (top) and the numerical simulations with the baseline model (middle) at $z = 10$ mm, colored with the radial positions. The conditional means at $z = 10$ mm is shown in the bottom row. The particles within 5 mm distance from the centerline are colored by black. Black solid line: the experiments; red dashed line: the simulations.

V. CONCLUSION

LES/PDF simulations have been applied to the Cambridge/Sandia stratified turbulent flames under swirling conditions employing finite-rate chemistry. The premixed (SwB3), the moderately stratified (SwB7), and the highly stratified (SwB11) flames are calculated using the identical models and parameters. In the simulations with the baseline model parameters, the resolved mean and the rms velocity results are found to be in close agreement with the measurements. Moreover, the radial plots of the mean and the rms temperature, equivalence ratio, and species mass fractions from the simulations have also been found to be in good agreement with the experimental measurements.

The scatter plots and their conditional means from the simulations are found to be in close agreement with the experimental data. Entrainment of the lower equivalence ratio mixture from the downstream to the recirculation zone is under-predicted near the bluff-body surface at $z = 10$ mm but over-predicted at the further downstream locations for the two stratified cases. Consequently, the equivalence ratio and temperature are over-predicted near the bluff-body surface and under-predicted at further downstream locations. The lengths of the recirculation zone are approximately five times longer than those of the non-swirling conditions. A unique challenge of the swirling bluff-body stabilized flames is posed by the downstream boundary conditions, which can have a more significant impact on the composition of the recirculation zones under the swirling conditions.

The comparison of the results from the simulation using the models with and without differential diffusion has shown that the differential diffusion has a minor effect on the length of the recirculation zone and the mean and on the rms velocity and scalar profiles for SwB3, SwB7, and SwB11. Compared to the non-swirling conditions, the length of the recirculation zone is more influenced by the swirling conditions than the existence of a bluff body and the differential molecular diffusion.

The effect of heat loss from the bluff-body wall is examined through a parametric study. It is found that taking into account the heat loss from the bluff body significantly improves the prediction of the mean temperature and CO mass fraction close to the inlet. Additionally, the inclusion of heat loss is found to have a negligible impact on the results at further downstream locations.

DATA AVAILABILITY

The data that support the findings of this study are available from the corresponding author upon reasonable request.

REFERENCES

[1]M. R. Johnson, D. Littlejohn, W. A. Nazeer, K. O. Smith, and R. K. Cheng, "A comparison of the flowfields and emissions of high-swirl injectors and low-swirl injectors for lean premixed gas turbines," Proc. Combust. Inst. **30**, 2867 (2005).

[2]Y. Huang, H.-G. Sung, S.-Y. Hsieh, and V. Yang, "Large-eddy simulation of combustion dynamics of lean-premixed swirl-stabilized combustor," J. Propul. Power **19**, 782 (2003).

[3]T. Lieuwen and K. McManus, "Introduction: Combustion dynamics in lean-premixed prevaporized (LPP) gas turbines," J. Propul. Power **19**, 721 (2003).

[4]W. Meier, X. R. Duan, and P. Weigand, "Investigations of swirl flames in a gas turbine model combustor," Combust. Flame **144**, 225 (2006).

[5]F. Grinstein and C. Fureby, in 41st AIAA Aerospace Sciences Meeting and Exhibit, Reno, 2003.

[6]G. Bulat, W. P. Jones, and A. J. Marquis, "Large eddy simulation of an industrial gas-turbine combustion chamber using the sub-grid PDF method," Proc. Combust. Inst. **34**, 3155 (2013).

[7]Z. X. Chen, I. Langella, N. Swaminathan, M. Stöhr, W. Meier, and H. Kolla, "Large eddy simulation of a dual swirl gas turbine combustor: Flame/flow structures and stabilisation under thermoacoustically stable and unstable conditions," Combust. Flame **203**, 279 (2019).

[8]S. Roux, G. Lartigue, T. Poinsot, U. Meier, and C. Bérat, "Studies of mean and unsteady flow in a swirled combustor using experiments, acoustic analysis, and large eddy simulations," Combust. Flame **141**, 40 (2005).

[9]J. Galpin, A. Naudin, L. Vervisch, C. Angelberger, O. Colin, and P. Domingo, "Large-eddy simulation of a fuel-lean premixed turbulent swirl-burner," Combust. Flame **155**, 247 (2008).

[10]B. Fiorina, R. Vicquelin, P. Auzillon, N. Darabiha, O. Gicquel, and D. Veynante, "A filtered tabulated chemistry model for LES of premixed combustion," Combust. Flame **157**, 465 (2010).

[11]V. Moureau, P. Domingo, and L. Vervisch, "From large-eddy simulation to direct numerical simulation of a lean premixed swirl flame: Filtered laminar flame-PDF modeling," Combust. Flame **158**, 1340 (2011).

[12]W.-W. Kim, S. Menon, and H. C. Mongia, "Large-eddy simulation of a gas turbine combustor flow," Combust. Sci. Technol. **143**, 25 (1999).

[13]U. Stopper, M. Aigner, W. Meier, R. Sadanandan, M. Stöhr, and I. S. Kim, "Flow field and combustion characterization of premixed gas turbine flames by planar laser techniques," J. Eng. Gas Turbines Power **131**, 72 (2009).

[14]P. Weigand, W. Meier, X. R. Duan, W. Stricker, and M. Aigner, "Investigations of swirl flames in a gas turbine model combustor," Combust. Flame **144**, 205 (2006).

[15]A. Bonaldo and J. B. Kelman, "Experimental annular stratified flames characterisation stabilised by weak swirl," Combust. Flame **156**, 750 (2009).

[16]K.-J. Nogenmyr, P. Petersson, X. S. Bai, A. Nauert, J. Olofsson, C. Brackman, H. Seyfried, J. Zetterberg, Z. S. Li, M. Richter et al., "Large eddy simulation and experiments of stratified lean premixed methane/air turbulent flames," Proc. Combust. Inst. **31**, 1467 (2007).

[17]K.-J. Nogenmyr, C. Fureby, X. S. Bai, P. Petersson, R. Collin, and M. Linne, "Large eddy simulation and laser diagnostic studies on a low swirl stratified premixed flame," Combust. Flame **156**, 25 (2009).

[18]K.-J. Nogenmyr, P. Petersson, X. S. Bai, C. Fureby, R. Collin, A. Lantz, M. Linne, and M. Aldén, "Structure and stabilization mechanism of a stratified premixed low swirl flame," Proc. Combust. Inst. **33**, 1567 (2011).

[19]M. S. Sweeney, S. Hochgreb, M. J. Dunn, and R. S. Barlow, "The structure of turbulent stratified and premixed methane/air flames I: Non-swirling flows," Combust. Flame **159**, 2896 (2012).

[20]M. S. Sweeney, S. Hochgreb, M. J. Dunn, and R. S. Barlow, "The structure of turbulent stratified and premixed methane/air flames II: Swirling flows," Combust. Flame **159**, 2912 (2012).

[21]S. Nambully, P. Domingo, V. Moureau, and L. Vervisch, "A filtered-laminar-flame PDF sub-grid scale closure for LES of premixed turbulent flames. Part I: Formalism and application to a bluff-body burner with differential diffusion," Combust. Flame **161**, 1756 (2014).

[22]S. Nambully, P. Domingo, V. Moureau, and L. Vervisch, "A filtered-laminar-flame PDF sub-grid-scale closure for LES of premixed turbulent flames: II. Application to a stratified bluff-body burner," Combust. Flame **161**, 1775 (2014).

[23]F. Proch and A. M. Kempf, "Numerical analysis of the Cambridge stratified flame series using artificial thickened flame LES with tabulated premixed flame chemistry," Combust. Flame **161**, 2627 (2014).

[24]T. Brauner, W. P. Jones, and A. J. Marquis, "LES of the Cambridge stratified swirl burner using a sub-grid PDF approach," Flow, Turbul. Combust. **96**, 965 (2016).

[25]H. Turkeri, X. Zhao, S. B. Pope, and M. Muradoglu, "Large eddy simulation/probability density function simulations of the Cambridge turbulent stratified flame series," Combust. Flame **199**, 24 (2019).

[26]H. Zhang, T. Ye, G. Wang, P. Tang, and M. Liu, "Large eddy simulation of turbulent premixed swirling flames using dynamic thickened flame with tabulated detailed chemistry," Flow, Turbul. Combust. **98**, 841 (2017).

[27]Y. Xiao, Z. Lai, and W. Song, "Large eddy simulation of premixed stratified swirling flame using the finite rate chemistry approach," Int. J. Aerosp. Eng. **2019**, 1.

[28]P. Gruhlke, E. Inanc, R. Mercier, B. Fiorina, and A. M. Kempf, in Proceedings of the Combustion Institute, 2020.

[29]R. Mercier, C. Mehl, B. Fiorina, and V. Moureau, "Filtered wrinkled flamelets model for large-eddy simulation of turbulent premixed combustion," Combust. Flame **205**, 93 (2019).

[30]J. Xu and S. B. Pope, "PDF calculations of turbulent nonpremixed flames with local extinction," Combust. Flame **123**, 281 (2000).

[31]M. Muradoglu, K. Liu, and S. B. Pope, "PDF modeling of a bluff-body stabilized turbulent flame," Combust. Flame **132**, 115 (2003).

[32]R. Mokhtarpoor, H. Turkeri, and M. Muradoglu, "A new robust consistent hybrid finite-volume/particle method for solving the PDF model equations of turbulent reactive flows," Comput. Fluids **105**, 39 (2014).

[33]H. Wang and S. B. Pope, "Flame edge statistics in turbulent combustion," Proc. Combust. Inst. **33**, 1439 (2011).

[34]R. R. Tirunagari and S. B. Pope, "Characterization of extinction/reignition events in turbulent premixed counterflow flames using strain-rate analysis," Proc. Combust. Inst. **36**, 1919 (2017).

[35]R. R. Tirunagari and S. B. Pope, "LES/PDF for premixed combustion in the DNS limit," Combust. Theory Modell. **20**, 834 (2016).

[36]J. Kim and S. B. Pope, "Effects of combined dimension reduction and tabulation on the simulations of a turbulent premixed flame using a large-eddy simulation/probability density function method," Combust. Theory Modell. **18**, 388 (2014).

[37]M. Juddoo, A. R. Masri, and S. B. Pope, "Turbulent piloted partially-premixed flames with varying levels of O_2/N_2: Stability limits and PDF calculations," Combust. Theory Modell. **15**, 773 (2011).

[38]H. Turkeri, S. B. Pope, and M. Muradoglu, "A LES/PDF simulator on block-structured meshes," Combust. Theory Modell. **23**, 1 (2018).

[39]A. Yoshizawa, "Statistical theory for compressible turbulent shear flows, with the application to subgrid modeling," Phys. Fluids **29**, 2152 (1986).

[40]R. McDermott and S. B. Pope, "A particle formulation for treating differential diffusion in filtered density function methods," J. Comput. Phys. **226**, 947 (2007).

[41]R. Kee, G. Dixon-Lewis, J. Warnatz, M. Coltrin, and J. Miller, "A fortran computer code package for the evaluation of gas-phase multicomponent transport properties," Report No. SAND86-8246, Sandia National Laboratories, Livermore, CA, USA, 1986.

[42]P. P. Popov, H. Wang, and S. B. Pope, "Specific volume coupling and convergence properties in hybrid particle/finite volume algorithms for turbulent reactive flows," J. Comput. Phys. **294**, 110 (2015).

[43]See https://openfoam.org/version/2-3-0/ for OpenFOAM-2.3; 2014.

[44]M. Euler, R. Zhou, S. Hochgreb, and A. Dreizler, "Temperature measurements of the bluff body surface of a swirl burner using phosphor thermometry," Combust. Flame **161**, 2842 (2014).

[45]R. Zhou, S. Balusamy, M. S. Sweeney, R. S. Barlow, and S. Hochgreb, "Flow field measurements of a series of turbulent premixed and stratified methane/air flames," Combust. Flame **160**, 2017 (2012).

[46]C. J. Sung, C. K. Law, and J.-Y. Chen, "Augmented reduced mechanisms for NO emission in methane oxidation," Combust. Flame **125**, 906 (2001).

[47]S. B. Pope, "Computationally efficient implementation of combustion chemistry using in situ adaptive tabulation," Combust. Theory Modell. **1**, 41 (1997).

[48]L. Lu, S. R. Lantz, Z. Ren, and S. B. Pope, "Computationally efficient implementation of combustion chemistry in parallel PDF calculations," J. Comput. Phys. **228**, 5490 (2009).

[49]R. R. Tirunagari and S. B. Pope, "An investigation of turbulent premixed counterflow flames using large-eddy simulations and probability density function methods," Combust. Flame **166**, 229 (2016).

[50]J. C. Massey, I. Langella, and N. Swaminathan, "A scaling law for the recirculation zone length behind a bluff body in reacting flows," J. Fluid Mech. **875**, 699 (2019).